Physics Letters A 559 (2025) 130905

Contents lists available at ScienceDirect

Physics Letters A

journal homepage: www.elsevier.com/locate/pla

Letter

High-robust topological edge states in quasi-one-dimensional zigzag systems

Valerii Kachin [a], J.C. López Carreño [a,b], Magdalena Stobińska [a,*]

[a] Institute of Informatics, Faculty of Mathematics, Informatics and Mechanics, University of Warsaw, Banacha 2, Warsaw, 02–097, Poland
[b] Institute of Theoretical Physics, Faculty of Physics, University of Warsaw, Pasteura 5, Warsaw, 02–093, Poland

ARTICLE INFO

Communicated by M.Z. Wu

Keywords:
Topological phase
Edge states
Negative couplings
Synthetic flux
Topological protection

ABSTRACT

Topological edge states in one-dimensional systems typically rely on symmetry protection, making them vulnerable to multiple types of disorder. Here, we demonstrate the emergence of remarkably resilient topologically protected edge states in a quasi-one-dimensional zigzag structure where some lattice couplings are negative. These states maintain their nature despite simultaneous disorders in lattice couplings, variations in on-site phases and potentials, and dissipation. Using a novel approach to restore bulk-boundary correspondence, we establish a continuous mapping between our model and a "parental model" with restored chiral symmetry, enabling computation of a regularized topological invariant. We propose practical implementations using orbital-induced synthetic flux in photonic waveguide arrays, showing good agreement between coupled mode theory and full-wave simulations. Our results reveal new mechanisms for achieving topological protection without conventional symmetries, with potential applications across multiple physical platforms including photonic, acoustic, and mechanical metamaterials.

1. Introduction

Topologically protected one-dimensional edge states are quantum states of matter whose wave function is concentrated at the edges of a 1D lattice, and vanishes in its bulk. Lattice symmetries shield them from noise, crystal defects, or chemical composition changes [1,2]. Their energy levels lie inside the energy gap between the valence and conduction bands. These states not only provide insights into fundamental quantum phenomena [3–7] but also hold promise for applications ranging from fault-tolerant quantum computation [8–12], robust information processing [13–18] to topological sensing [19–23].

The Su-Schrieffer-Heeger (SSH) model stands as the archetypal example of topological edge states in one-dimensional systems, where protection stems from chiral symmetry [24–26]. When the intra-cell coupling exceeds the inter-cell coupling strength, topologically protected edge states emerge at the system boundaries. This foundational model has inspired numerous variations and generalizations [27–32], studying edge states in quasicrystal structures [33–35], the Aubry–André–Harper model [36,37], and Anderson topological insulators [38,39]. However, most of these systems rely heavily on specific symmetries for protection, making them vulnerable when multiple types of disorder coexists [40,41].

While previous approaches demonstrate robustness against individual types of disorder, achieving protection against multiple simultaneous disorders remains an outstanding challenge [42–45]. Moreover, most existing systems rely heavily on specific symmetries for protection, limiting their practical applications [46–48].

Negative couplings have emerged as a versatile tool for realizing non-trivial topological phases and opening energy gaps in a variety of physical systems, including photonic, acoustic, atomic, and electrical platforms [49–57]. Negative couplings naturally arise in systems such as ultracold atoms in optical lattices [58,59], microwave resonator arrays [50,60], optical waveguide lattices [51,56,57,61–66], acoustic cavities [53,54,67], synthetic dimensions [68,69], and topolectrical circuits [70,71]. Recent advances have shown that introducing negative couplings and artificial magnetic flux enables the realization of exotic topological phenomena, such as Aharonov-Bohm caging, flat bands, and compact localized states [52,54,65,66,72–79].

Here we demonstrate remarkably resilient topologically protected edge states in a quasi-one-dimensional system with negative couplings, extending previous approaches that focused primarily on nearest-neighbor interactions. Unlike previous designs, our approach achieves robust edge states without relying on conventional symmetries, main-

* Corresponding author.
E-mail address: magdalena.stobinska@gmail.com (M. Stobińska).

https://doi.org/10.1016/j.physleta.2025.130905
Received 12 May 2025; Received in revised form 10 August 2025; Accepted 16 August 2025

Available online 25 August 2025

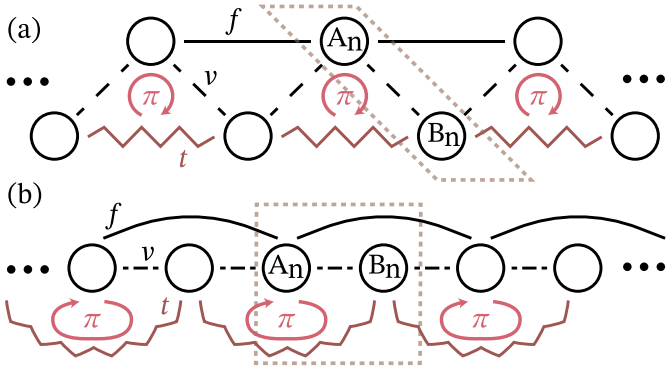

Fig. 1. Two equivalent representations of the zigzag topological chain. (a) Physical realization showing two interacting chains A and B with coupling strengths f (black line) and t (red zigzag line), and interchain coupling $v > 0$ (dashed line). Flux π threading half of each unit cell. (b) Transformed representation highlighting the nearest-neighbor (v) and next-nearest-neighbor (f, t) interactions. The dotted frame indicates the elementary two-site unit cell preserving the topology of the system.

taining protection against simultaneous disorders in lattice couplings, on-site potentials, and dissipation.

Through analytical mapping to a "parental model," we restore bulk-boundary correspondence and compute a regularized topological invariant, providing theoretical understanding of the protection mechanism. Negative couplings prove crucial for edge state stabilization, localization control, and energy gap formation. We propose practical implementations using orbital-induced synthetic flux in photonic waveguide arrays, demonstrating excellent agreement between coupled mode theory and full-wave simulations. Our approach extends beyond photonics, suggesting implementations in acoustic metacrystals, superconducting circuits, and resonant electric networks.

The paper is organized as follows. In Section 2, we present our theoretical model and establish its topological properties through mapping to a ladder system with restored chiral symmetry. Section 3 demonstrates the remarkable robustness of edge states against various forms of disorder. Section 4 details our proposed physical implementation using photonic waveguide arrays with orbital-induced synthetic flux, while Section 5 explores device operation through both edge states and engineered defect states. Finally, Section 6 discusses broader implications and potential extensions of our work.

2. Design and theoretical model

2.1. System design and Hamiltonian

We consider a zigzag chain with nearest and next-nearest neighbor interactions, i.e., a quasi-one-dimensional lattice composed of two interconnected topologically trivial chains, A and B (see Fig. 1a). The unit cell is threaded halfway by a flux of π. The moment space Hamiltonian describing this system is given by

$$H(k) = \begin{pmatrix} 2f\cos k & v\left(1+e^{-ik}\right) \\ v\left(1+e^{ik}\right) & e^{i\pi}2t\cos k \end{pmatrix}, \tag{1}$$

where v is the hopping amplitude between chains A and B, and f (t) is the hopping amplitude within chain A (B). For simplicity, instead of mentioning the phase $e^{i\pi}t$, we will assume that the parameter $t \leq 0$. The system can be viewed as a chain with uniform nearest-neighbor (nn) interactions and two opposite-phase strengths of next-nearest-neighbor (nnn) interactions (see Fig. 1b). Long-range repulsive and attractive interactions make this model distinct from the standard SSH and AAH models and determine its non-trivial topological properties, which will be discussed later. Without these interactions, the system becomes a topologically trivial gapless chain.

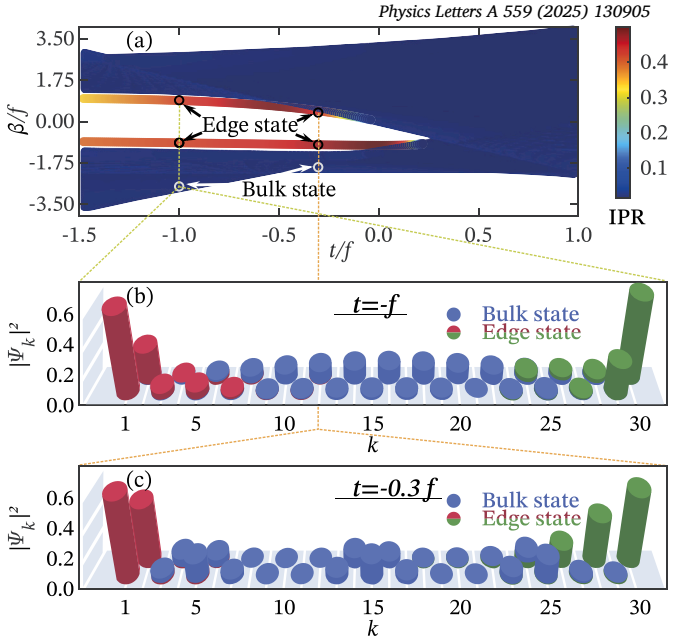

Fig. 2. Energy Spectrum and Spatial Profiles of Edge and Bulk States. (a) Energy band structure of the zigzag system ($N = 30$ sites, $v/f = 1$) as a function of the interaction strength ratio t/f. The states are colored by their inverse participation ratio (IPR), highlighting the localized edge states. (b) At the chiral symmetric point $t/f = -1$, the system supports two symmetric edge states whose wavefunction intensities, localizing at opposite boundaries of the chain. (c) With broken chiral symmetry at $t/f = -0.3$, the two edge states (one at the left boundary, red, and one at the right boundary, green) are no longer symmetric. In both cases, representative bulk states (blue) are shown to be delocalized across the lattice.

The spectrum of $H(k)$ has two bands at energies

$$\varepsilon_{\pm} = (f+t)\cos k \pm \sqrt{(f-t)^2\cos^2 k + 2v^2(1+\cos k)}.$$

It returns conditions for gap closure (see Appendix A):

$$v^2 \leq (f+t)(f+t-|f-t|) \qquad \text{and} \qquad f = t.$$

Negative coupling ($t < 0$) is crucial, as it maintains a robust energy gap and directly leads to the formation of topologically protected edge states, the emergence and nature of which presented in Fig. 2. Panel (a) displays the energy spectrum as a function of the hopping ratio t/f. Here, the inverse participation ratio (IPR) is used as a color map, which clearly distinguishes the highly localized edge states (red/yellow) from the delocalized bulk states (blue) and shows the robust presence of edge states within the energy gap for $t < 0$.

The defining characteristic of these topological states is explicitly illustrated for two representative cases. In Fig. 2(b), we examine the special point t = -f, which possesses an additional chiral symmetry (this will be discussed in Subsection 2.3). At this point, the system supports two edge states whose wavefunction intensities, are symmetric to each other, localizing at opposite boundaries of the chain. All cases with $t \neq -f$ symmetry is broken and the two edge states persist but are no longer symmetric as shown in Fig. 2(c) for $t = -0.3f$. One state localizes at the left boundary (red, $\beta < 0$) and the other at the right boundary (green, $\beta > 0$), with different energies. This demonstrates the general and robust nature of these states while highlighting their non-trivial structure, which contrasts starkly with the delocalized bulk states (blue) shown in both panels, demonstrating strong confinement to the few sites of the edges of the chain. This stands in stark contrast to a typical bulk state (blue), which is delocalized across the entire lattice.

2.2. Open chain

The rich behavior visualized in Fig. 2 provides the foundation for our analytical treatment. Unlike conventional topological systems where gap closure and reopening lead to edge states on one side and nothing on the other, our zigzag system exhibits a more nuanced behavior. Analysis of the open chain reveals that for parameter regimes satisfying $t < v^2/(4f)$, the system supports edge states with energies in the gap (see Appendix B), which perfectly align with Fig. 2. While a general closed-form analytical solution for the localization parameter in terms of the coupling parameters f, t, and v appears intractable, we can fully characterize these edge states analytically for specific coupling combinations (e.g., $t = 0$ or $t = -f$).

2.3. Topological properties

The robustness of edge states in practical implementations depends critically on the system's topological properties and protection mechanisms. Due to the lack of chiral, inversion, or mirror symmetry in the general unit cell, the evaluated 1D topological invariant (Zak's winding phase) does not take a quantized value for each band. This contrasts with the standard 1D SSH model, where the winding phase takes only quantized values of π (or 0).

Introducing a $t = -f$ condition, the unit cell obtains the chiral symmetry $\Gamma_2 = \sigma_y K$ where σ_y is Pauli matrix and K is time-reversal operator:

$$\sigma_y = \begin{pmatrix} 0 & -i \\ i & 0 \end{pmatrix} \tag{2}$$

Notwithstanding chiral symmetry in this special case, the winding number is still not quantized: which aligns well with the fact that the inversion axis is non-centered, shifted to one of the sites in the unit cell. This result is consistent with the dynamical measurement of the mean chiral displacement proposed by Jiao et al. [80]; the lack of inversion symmetry within the unit cell would similarly prevent the observation of a quantized displacement, suggesting that the edge states' robustness stems from a different mechanism than conventional symmetry protection.

To establish a rigorous theoretical foundation for the observed robustness, we show that the topological origin of the model can be restored with a continuous transformation $w \to 0$ (it happens without closing the main energy gap, as shown in Fig. 3(a)) in a four-site (instead of two-site) unit cell, as shown at Fig. 3(b). We name resulting system with $w = 0$ a parental ladder model, featuring the chiral symmetry $\Gamma_4 = \sigma_z \otimes I_2$ with Pauli matrix σ_z and 2×2 identity matrix:

$$\sigma_z = \begin{pmatrix} 1 & 0 \\ 0 & -1 \end{pmatrix} \qquad I_2 = \begin{pmatrix} 1 & 0 \\ 0 & 1 \end{pmatrix}. \tag{3}$$

Constructing the momentum space Hamiltonian H_4^{ladder} of the ladder system requires projecting interaction between upper and lower chains (perpendicular to the momentum direction in the general case). This can be done in two possible ways, corresponding to two choices of four-site unit cells, $\diagup$ and $\diagdown$ (Fig. 3(c) and(d), respectively). Considering only one of these projections leads to a non-converging winding integral. Therefore, we introduce the concept of a weighted unit cell Hamiltonian, which allows the construction of a well-converging winding phase, taking into account both unit cell configurations shown in Fig. 3(c) and (d):

$$H_4^{ladder} = \frac{H_4\left(\diagup\right) + \xi H_4\left(\diagdown\right)}{\xi + 1}, \tag{4}$$

in the Γ_4 basis with properties determined by the upper-right block

$$h_2(k,\xi) = \begin{pmatrix} f\left(1 + e^{-ik}\right) & v\frac{e^{-ik} + \xi e^{ik}}{\xi + 1} \\ v & t\left(1 + e^{-ik}\right) \end{pmatrix}. \tag{5}$$

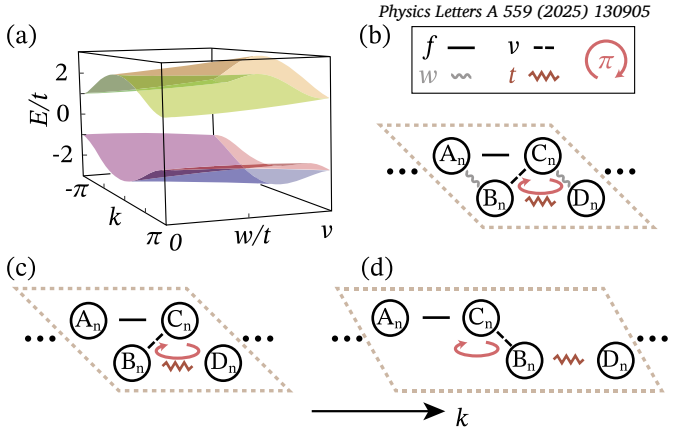

Fig. 3. Topological transition in the generalized zigzag model. We generalize the zigzag model by allowing the chains A and B to interact with two alternating strengths, v and w. (a) Energy band structure $E(k)/t$ showing gap preservation during w-parameter evolution. (b) Four-site unit cell structure with coupling legend. If $w = 0$, the model amounts to a ladder with four-site non-trivial unit cell. (c) and (d) Two equivalent projections of the ladder configuration at $w = 0$. Unit cells at (c) and (d) correspond to Hamiltonians $H_4\left(\diagup\right)$ and $H_4\left(\diagdown\right)$, respectively.

It also governs the winding number which takes the form

$$W = \frac{1}{i2\pi}\int_{BZ} dk \mathrm{Tr}\left(h_2(k,\xi)^{-1}\frac{d}{dk}h_2(k,\xi)\right) =$$

$$= \int_0^{2\pi} \frac{dk}{2\pi} \frac{\frac{2ft}{v^2}(\xi+1)\left(1+e^{-ik}\right) + \left(\xi e^{2ik} - 1\right)}{\frac{2ft}{v^2}(\xi+1)(1+\cos k) - \left(\xi e^{2ik} + 1\right)}. \tag{6}$$

For $\xi \ll 1$, the integral in W does not converge. However, larger values of ξ lead to the identification of non-trivial region, namely $W = 1$ for $t \in (-\infty; v^2/(4f))$ and $W = 0$ for $t \in [v^2/(4f); \infty)$.

3. Robustness of topological edge states

The theoretical framework established above provides a foundation for understanding the remarkable robustness of our system. While conventional topological protection relies on specific symmetries, our approach using negative couplings and the restored bulk-boundary correspondence through the parental model suggests protection should persist even under multiple types of disorder. In the following section, we demonstrate this exceptional robustness through systematic analysis of various perturbations.

The considered zigzag chain, with flux π and open boundary conditions, supports two in-gap nonzero energy states localized at opposite boundaries. These states inherit spatial properties from the four-way generalized chirality of the four-site unit cell $\mathbb{\Gamma}_4^4 = I$:

$$\mathbb{\Gamma}_4^{-1} H(k) \mathbb{\Gamma}_4 + \mathbb{\Gamma}_4^{-2} H(k) \mathbb{\Gamma}_4^2 + \mathbb{\Gamma}_4^{-3} H(k) \mathbb{\Gamma}_4^3 = -H(k) \tag{7}$$

$$H(k) = \begin{pmatrix} 0 & v & & h_2(k,0) \\ v & 0 & & \\ & & 0 & v \\ h_2(k,0)^\dagger & & v & 0 \end{pmatrix}, \mathbb{\Gamma}_4 = \sigma_z \otimes \begin{pmatrix} 1 & 0 \\ 0 & i \end{pmatrix}. \tag{8}$$

This symmetry results in the localization of nonzero edge states on three out of the four sublattices, without closing the gap. It is quite surprising that in our case, where the winding number is not directly quantized, these states remain robust in terms of both localization and energy, despite disorders in nn and nnn interactions, as well as on-site potentials typically associated with symmetry-protected bands that possess a quantized topological index (Fig. 4(a) and (b)).

To systematically analyze the system's resilience to realistic imperfections, we consider three fundamental types of disorder that com-

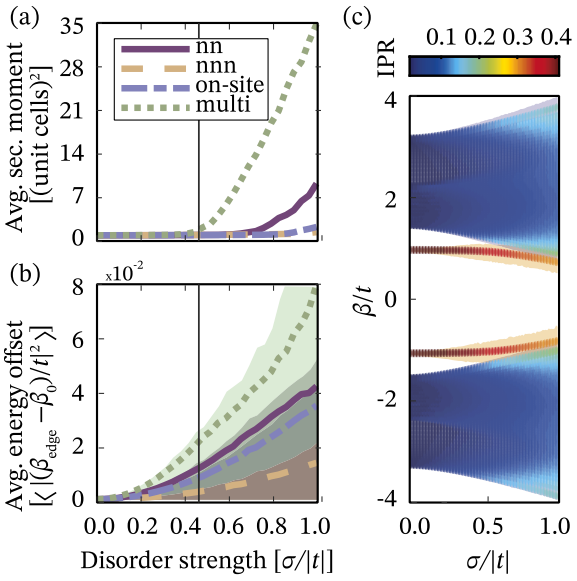

Fig. 4. Disorder analysis of edge states ($t/f = -1$, $v/f = 1$). (a) Average second moment showing spatial spreading vs disorder strength. A vertical line marks the energy gap separating the edge state from the nearest bulk band. (b) Mean squared deviation of edge state energy (β_{edge}) from unperturbed values (β_0). (c) IPR heat map demonstrating bulk-edge separation in the system with combined disorder, as a function of the disorder strength. Disorder types: nearest-neighbor (nn), next-nearest-neighbor (nnn), on-site potential, and combined (multi). These disorder-averaged simulations with standard deviations employed a 90-site lattice, with each disorder strength iterated 10,000 times.

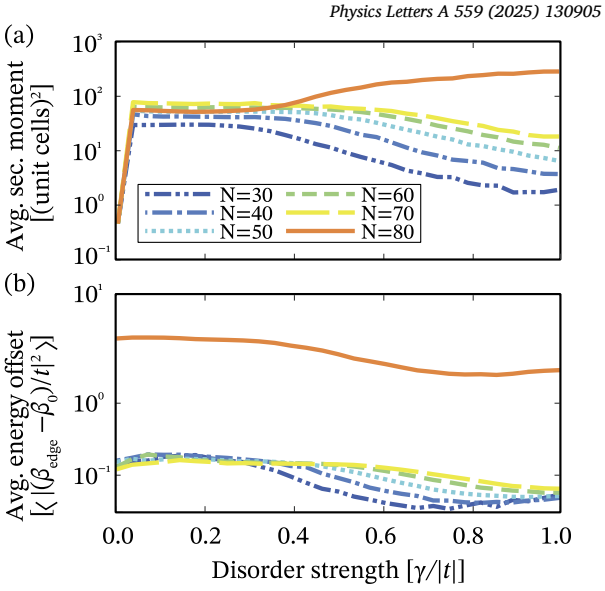

Fig. 5. Size-dependent loss disorder analysis ($f/t = -0.5$, $v/t = -0.8$). (a) Effect of loss disorder on edge state localization for varying system sizes N. Note logarithmic scale for second moment. (b) Energy offset showing distinct behavior for $N > 70$ where gap collapse occurs. Each disorder strength averaged over 10,000 iterations.

monly arise in photonic implementations. Disorders are defined as follows: let $H_\sigma = H + \sigma D$ denote the perturbed finite Hamiltonian, where H is the finite tight-binding Hamiltonian of the unperturbed system, σ is a constant quantifying the disorder strength, and D is a matrix defining the disorder type. The matrix elements are defined as:

1. $D_{l,m} = \Delta d\,\delta_{l\pm1,m}$ for disorder in nearest-neighbor (nn) coupling constants
2. $D_{l,m} = \Delta d\,\delta_{l\pm2,m}$ for disorder in next-nearest-neighbor (nnn) coupling constants
3. $D_{l,m} = \Delta d\,\delta_{l,m}$ for spectral disorder

Combined disorder, labeled as "multi" in Fig. 4, represents the sum of these individual disorders. In all cases, Δd is sampled uniformly from the range $[-0.5, 0.5]$.

Our analysis reveals that boundary modes exhibit resilience to various disorder types when the average disorder is zero. This robustness is evident in both energy and localization until the disorder intensity reaches a level to mix the boundary states with the nearest bulk band (Fig. 4(c)), which could be seen with inverse participation ratio (IPR, see Appendix C) analysis.

The robustness of edge states in the zigzag system persists for various f/t and v/t parameters with an even number of sites. The average second moment and energy offset significantly change only when the disorder strength approaches the energy gap between the boundary state and the nearest bulk band. In chains with odd N, edge states exhibit degenerate energy levels and disorder levels, still below the energy gap, causing only minor spectral spreading of these states.

Another type of imperfection in real devices is associated with varying on-site dissipation, which can arise from material absorption, scattering losses, and fabrication-induced variations in waveguide geometry. This can be modeled using a finite non-Hermitian Hamiltonian $H_\gamma = H + i\gamma D'$, where γ represents loss strength and D' is a diagonal matrix with elements $D_{l,m} = \Delta d\,\delta_{l,m}$. We sample Δd uniformly from $[-0.5; 0.5]$.

Our analysis reveals that the stability of edge states and the energy gap in the studied zigzag system under dissipation disorder depend on the number of sites, N. Fig. 5 illustrates that as N increases, the traced edge state disappears due to the collapse of the energy gap. This occurs for the model with parameters $v/t = -0.8$ and $f/t = -0.5$ at $N = 80$. Up to $N = 70$, the model exhibits similar behavior in the average second moment and energy offset as functions of the loss strength $\gamma/|t|$. Surprisingly, the influence of loss disorder on the edge state decreases with increasing loss strength.

These findings provide clear design guidelines for experimental implementations: while the system shows remarkable robustness, practical devices should be designed with carefully chosen N, v/t and f/t ratios to maintain topological protection. Notably, losses do not break the degeneracy of edge states in systems with odd N, offering an additional design consideration for specific applications.

4. Physical implementation design

The theoretical model presented in previous sections requires three key elements for practical realization: (1) a mechanism for achieving negative couplings, (2) precise control over coupling strengths to maintain the conditions derived in Section 2.1, and (3) the ability to create an effective flux π threading. The photonic waveguide implementation we propose here accomplishes all three requirements through orbital-induced synthetic flux [56,57,62]. By exploiting the coupling between fundamental (s) and second-order (d) modes, we can naturally achieve the negative coupling essential for our theoretical predictions while maintaining the required phase relationships. The waveguide parameters are carefully chosen to satisfy the gap conditions derived in Section 2.1, ensuring robust topological protection.

Our design employs an array of fourfold symmetric waveguides with square cross-sections, as illustrated in Fig. 6(a). The fundamental mode profiles at the operating wavelength $\lambda = 1.55$ μm are shown in Fig. 6(b). The design provides practical control mechanisms for different types of disorder studied theoretically: coupling noise can be adjusted through waveguide spacing, on-site energy variations through waveguide widths, and losses through waveguide etch depth.

The waveguide parameters are carefully chosen to match the theoretical requirements while remaining within practical fabrication con-

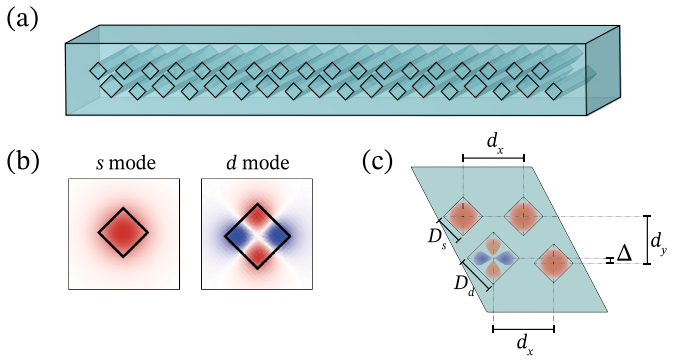

Fig. 6. Photonic waveguide orbital-induced synthetic flux implementation. (a) 3D schematic showing zigzag lattice structure. (b) Fundamental mode profiles (E_x at $\lambda = 1.55$ μm) for square waveguides supporting s and d modes. Refractive indices: $n_s = 1.5428$, $n_d = 1.5461$, cladding $n_{cl} = 1.54$. (c) Unit cell geometry with coupling control parameters: waveguide dimensions $D_s = 10.5$ μm, $D_d = 14$ μm; center-to-center distances $d_x = 23$ μm, $d_y = 18$ μm; diagonal shift $\Delta = 2$ μm.

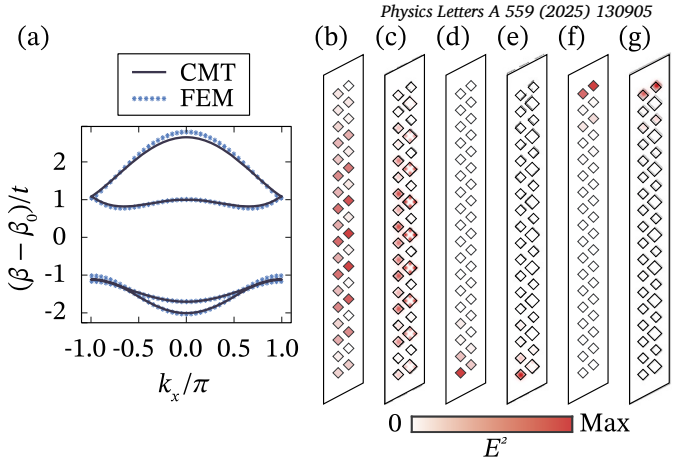

Fig. 7. Comparison between CMT and FEM simulations ($v/t = -0.8$, $f/t = -0.5$). (a) Band structure: CMT (black lines) vs FEM results (blue stars). (b-g) Field intensity distributions (E^2) in a 36-site lattice: (b,c) bulk mode from CMT and FEM; (d,e) first edge mode; (f,g) second edge mode. Red indicates higher field intensity.

straints. Individual s and d modes are designed to have nearly identical propagation constants ($\beta_0 = 6.25$ μm^{-1}, with differences of order 10^{-8} μm^{-1}) using the following parameters:

- s-waveguide: side length $D_s = 10.5$ μm, refractive index $n_s = 1.5428$
- d-waveguide: side length $D_d = 14$ μm, refractive index $n_d = 1.5468$
- Cladding refractive index: $n_{cl} = 1.54$

The unit cell geometry, shown in Fig. 6(c), achieves the required coupling strengths through specific spatial parameters: $d_x = 23$ μm, $d_y = 18$ μm, and a diagonal shift $\Delta = 2$ μm. This configuration, particularly the Δ shift, ensures equal diagonal coupling between s-s and s-d waveguides, a critical requirement for realizing our theoretical model.

The coupling strength is determined by the relation:

$$|c| = \sqrt{(\beta_0 - \beta_1)(\beta_2 - \beta_0)}, \tag{9}$$

derived from a two-waveguide coupler Hamiltonian, where β_1 and β_2 are the propagation constants of the coupler (see Appendix D). This approach provides a more precise estimation of coupling magnitudes than the overlap of decoupled base states. However, to determine the sign of the coupling, we still rely on the overlap integration of the decoupled base states [81].

The design presented supports a band gap and edge states that align with our theoretical model, as demonstrated through comprehensive numerical analysis. We validated our implementation through two complementary approaches: coupled mode theory (CMT) and full-wave finite element method (FEM) simulations. Our CMT analysis reveals coupling values of $v/t = -0.8$ and $f/t = -0.5$, placing the system in the parameter regime where theoretical analysis predicts robust topological protection. The comparison between CMT and FEM results shows excellent agreement, as evidenced in the bulk bands comparison in Fig. 7(a). A slight offset observed in the band structure can be attributed to next-nearest-neighboring coupling between d-d waveguides when studying the bottom lattice line separately - an effect that disappears when $\Delta = 0$ μm.

The edge state analysis reveals an even richer correspondence between theory and simulation. Edge states in the photonic waveguide structure can form with either s or d waveguides at the boundaries, exhibiting localization characteristics that match CMT predictions with remarkable precision (Fig. 7(b)-(g)). The bulk state behavior, shown in Fig. 7(b) and (c) for CMT and FEM cases respectively, demonstrates consistent field distributions. Furthermore, the use of an even number of sites breaks global inversion symmetry, resulting in two non-zero states with opposite energies and distinct localization profiles - a key prediction of our theoretical model. This behavior is clearly visible in both CMT calculations (Fig. 7(d) and (f)) and FEM simulations (Fig. 7(e) and (g)), providing strong validation of our implementation approach.

5. Device operation and performance verification

Having established the physical implementation design, we now demonstrate the operational characteristics of our device, focusing on its ability to maintain robust light propagation even in the presence of disorder. Our analysis involves both conventional edge state operation and an engineered defect configuration (Fig. 8(a,b)), where the latter is created by canceling the coupling between two neighboring sites in the bottom chain. In the waveguide lattice, this defect is implemented through a three-level system while maintaining the original waveguide parameters.

We examine the device dynamics through coupled mode calculations based on Helmholtz equations, leveraging the validated agreement between CMT and FEM results from our implementation analysis. Our simulations focus on a practical 36-site system, incorporating combined disorder in couplings and on-site potentials with strength $\sigma/|t| = 0.5$ to mimic real-world fabrication imperfections.

5.1. Edge state operation

Light propagation at the device boundaries demonstrates the robust operation of topological edge states. As shown in Fig. 8(c), light injected at the upper boundary remains strongly localized to the first two sites with minimal bulk spreading, maintaining its intensity profile despite the presence of disorder. Similarly, injection at the lower boundary (Fig. 8(d)) exhibits strong confinement to the terminal sites, with maximum intensity preserved at the injection point throughout propagation. These results confirm that the topological protection predicted by our theoretical analysis translates into practical device operation.

5.2. Engineered defect states

Building upon the defect design introduced earlier, we demonstrate how such engineered states can provide additional functionality for light control. The defect state (Fig. 8(e)) exhibits localization characteristics similar to natural edge states, with intensity spread limited to just 5 sites and maximum intensity maintained at the injection site.

For comparison, we examined bulk state propagation (Figs. 8(f,g)) from sites 20 and 19. The observed significant intensity spreading and dispersive pattern highlights the unique confinement properties of both

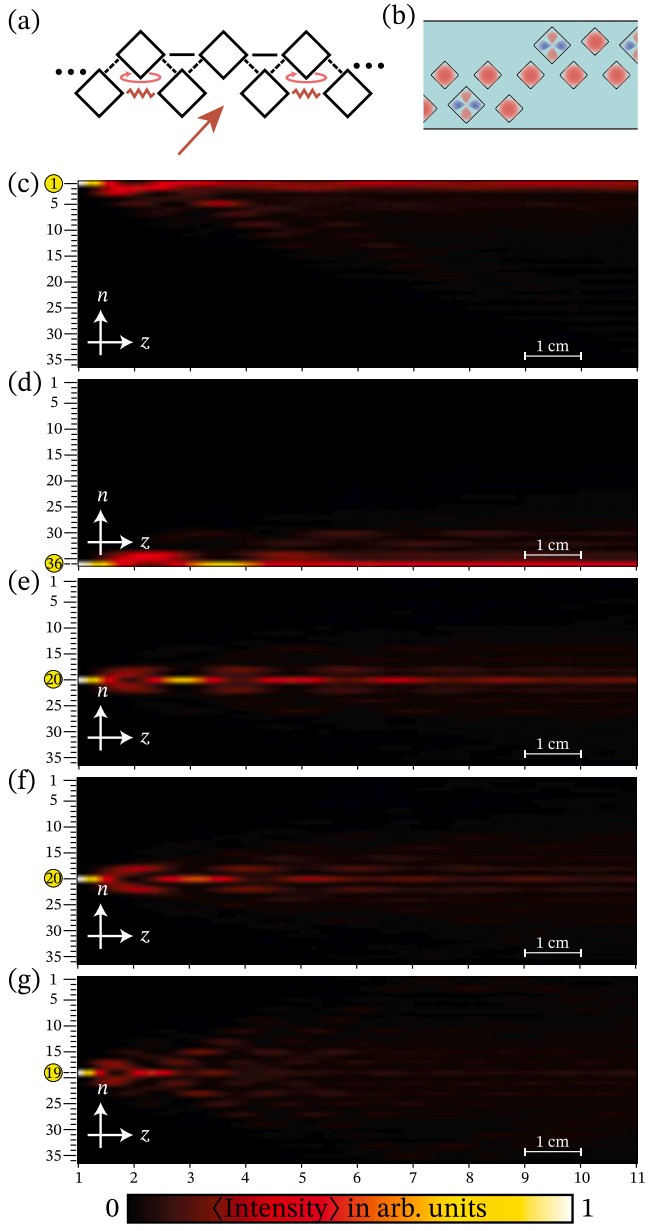

Fig. 8. Coupled mode dynamics with disorder (36-site lattice, $\sigma/|t| = 0.5$, 1000 iterations). (a) Schematic of a defect configuration. (b) Waveguide defect implementation. (c-g) Averaged intensity evolution of an initially excited wavepacket: (c,d) edge state dynamics from opposite boundaries; (e) defect state dynamics; (f,g) bulk state propagation. Yellow circles mark injection sites. Intensity normalized to initial value. The vertical axis represents the discrete waveguide position ($n = 1, 2, ..., 36$), and the horizontal axis corresponds to the propagation distance ($0 \le z \le 11$ cm).

edge and defect states, demonstrating their potential for controlled light manipulation in practical devices.

6. Discussion and conclusion

Our investigation reveals a fundamental new mechanism for achieving topological protection in quasi-1D systems without relying on conventional symmetries. The remarkable simultaneous robustness against coupling disorders, on-site potentials, and dissipation stems from the interplay between nn- and nnn-interactions with negative couplings (or the flux π threading), which maintains topological protection even when multiple types of disorder coexist. This mechanism differs fundamentally from traditional symmetry-based protection schemes, offering a distinct advantage in maintaining robustness under general disorder conditions and thus enhancing its relevance for practical implementations where such symmetries are not preserved. While our focus has been on zigzag chains, the weighted unit cell Hamiltonian approach introduced here has potential applications to a broader class of quasi-1D systems with complex unit cells and vertical connections perpendicular to the momentum direction. Preliminary analyses suggest it can be effectively applied to characterize topological phases in systems like SSH-Stub chains [82], SSH4 [83] and coupled SSH ladders [84], providing a mathematical foundation for establishing the topological nature of previously observed but incompletely understood edge states in these systems.

The practical validation through waveguide arrays demonstrates both opportunities and challenges for experimental implementation. While our theoretical predictions show excellent agreement with coupled mode and full-wave simulations, several engineering challenges need careful consideration. The response to dissipative disorder varies with system size, requiring careful optimization of device dimensions. The requirement for square-profile waveguides to properly utilize the second-order d-mode presents fabrication challenges - the femtosecond laser pulses typically used result in rounded profiles due to the Gaussian beam nature. These imperfections manifest as systematic variations in waveguide profiles and coupling strengths across the lattice. Though our system demonstrates robustness to sub-linear gradients, stronger lattice-wide variations could compromise protection.

The fundamental nature of our approach suggests implementations beyond photonics. The key requirement of negative couplings can be achieved through various physical mechanisms: the orbital-induced synthetic flux scheme could be adapted for circular waveguides with careful management of the degenerate d orbital; effective negative coupling could be realized through auxiliary defect waveguides with precisely tuned refractive indices; acoustic metacrystals could employ 3D-printed structures with specially designed unit cell connections [53]; superconducting circuits could utilize SQUIDs and magnetic flux for coupling control [85]; and resonant electric circuits could implement the necessary coupling scheme through appropriate combinations of capacitors and inductors.

The marriage of theoretical insight with practical implementation demonstrated here suggests a promising path toward next-generation topological devices that maintain functionality despite significant imperfections.

CRediT authorship contribution statement

Valerii Kachin: Writing – review & editing, Writing – original draft, Visualization, Software, Methodology, Investigation, Conceptualization. **J.C. López Carreño:** Formal analysis. **Magdalena Stobińska:** Writing – review & editing, Writing – original draft, Validation, Supervision, Resources, Project administration, Methodology, Funding acquisition, Conceptualization.

Declaration of competing interest

The authors declare that they have no known competing financial interests or personal relationships that could have appeared to influence the work reported in this paper.

Acknowledgements

V.K. thanks Alexander Khanikaev for the initial discussions and Diana Shakirova for the FEM calculation discussions. We are grateful to the anonymous reviewers whose insightful comments and suggestions led to important additions in the introduction, design and theoretical model, and discussion sections, strengthening the presentation and broadening the context of this work. V.K. and M.S. were supported by the European Union's Horizon 2020 research and innovation programme

under the Marie Skłodowska-Curie project "AppQInfo" No. 956071. M.S. was supported by the National Science Centre "Sonata Bis" project No. 2019/34/E/ST2/00273, and the QuantERA II Programme that received funding from the European Union's Horizon 2020 research and innovation programme under Grant Agreement No. 101017733, project "PhoMemtor" No. 2021/03/Y/ST2/00177.

Appendix A. Gap closure conditions

The energy spectrum is given by $\epsilon_{\pm}(k) = A(k) \pm B(k)$, where $A(k) = (f+t)\cos k$ and $B(k) = \sqrt{(f-t)^2\cos^2 k + 2v^2(1+\cos k)}$. The energy gap is defined as $\Delta = \min_{k_1} \epsilon_+(k_1) - \max_{k_2} \epsilon_-(k_2)$. Gap closure occurs when $\Delta \leq 0$.

A.1. Touching condition ($f=t$)

Direct band touching requires $\epsilon_+(k) = \epsilon_-(k)$ for some k, implying $B(k) = 0$. Assuming $v \neq 0$, this necessitates $1+\cos k = 0$ (i.e., $k = \pm\pi$) and simultaneously $(f-t)^2\cos^2 k = 0$, which leads to $(f-t)^2 = 0$. The touching condition is therefore:

$$f = t. \tag{A.1}$$

A.2. Overlap condition ($f \neq t$)

Overlap, corresponding to $\Delta \leq 0$, can occur if $\min \epsilon_+ \leq \max \epsilon_-$. Comparing the typical extrema candidates $\epsilon_+(\pi) = -(f+t) + |f-t|$ and $\epsilon_-(0) = f + t - \sqrt{(f-t)^2 + 4v^2}$, the condition $\epsilon_+(\pi) \leq \epsilon_-(0)$ leads to the requirement:

$$v^2 \leq (f+t)(f+t-|f-t|). \tag{A.2}$$

Solving the boundary defined by Eq. (A.2) for t, assuming real parameters f, t, v and specifically $f > t$, yields the condition represented as:

$$t \leq \frac{1}{2}\left(\sqrt{f^2+2v^2} - f\right). \tag{A.3}$$

Appendix B. Edge state analysis for open chain

To analyze the emergence of edge states in our zigzag lattice model, we consider a half-infinite system with boundary conditions on the left side of the chain:

$$\begin{cases} A_0 = 0 \\ B_0 = 0 \end{cases} \tag{B.1}$$

For systems exhibiting localized edge states, we employ the ansatz $\{A_{j+1}, B_{j+1}\} = \{\alpha, \beta\} s^j \exp(i\Omega z)$, where α and β relate to normalization, s is a localization parameter ($|s| \leq 1$), and Ω denotes the energy. Substituting this ansatz into the equations of motion yields:

$$\Omega\alpha s - f\alpha(1+s^2) - v\beta(1+s) = 0 \tag{B.2a}$$

$$\Omega\beta s - t\beta(1+s^2) - v\alpha(s+s^2) = 0 \tag{B.2b}$$

Incorporating the boundary conditions:

$$\Omega\alpha - f\alpha s - v\beta = 0 \tag{B.3a}$$

$$\Omega\beta - t\beta s - v\alpha(1+s) = 0 \tag{B.3b}$$

From the first equation, we express the boundary energy:

$$\Omega = fs + v\frac{\beta}{\alpha} \tag{B.4}$$

Introducing the ratio $\delta = \frac{\alpha}{\beta}$ and substituting into equation (B.3b) gives:

$$\left(fs + \frac{v}{\delta}\right) = ts + v\delta(1+s) \tag{B.5}$$

Solving for the localization parameter s and energy Ω:

$$s = \frac{v(1-\delta^2)}{\delta^2 v + \delta(t-f)}, \quad \Omega = \frac{\delta v^2 + vt - \delta^2 fv}{\delta^2 v + \delta(t-f)} \tag{B.6}$$

In special cases, we can derive explicit solutions. For $t = 0$, we find $\delta = -v/f$, yielding:

$$s = \frac{f^2 - v^2}{f^2 + v^2}, \quad \Omega = \frac{-2fv^2}{f^2+v^2} \tag{B.7}$$

For $f = -t$, with $\delta = \frac{-v+\alpha}{2f}$ where $\alpha = \sqrt{v^2+4f^2}$:

$$s = \frac{-2v^2}{\alpha^2 + v\alpha}, \quad \Omega = \frac{-2vf}{\alpha} \tag{B.8}$$

While a general closed-form analytical solution in terms of f, t, and v appears intractable, we can generalize the parameter as $\alpha = \sqrt{v^2 - 4ft}$. For the energy eigenvalue to remain real with real-valued coupling parameters, we require:

$$v^2 - 4ft > 0 \tag{B.9}$$

This constraint ($t < \frac{v^2}{4f}$ for positive f and v) establishes the parameter regime supporting localized edge states in our zigzag lattice model.

Appendix C. Inverse participation ratio

To quantify mode localization properties, we calculate an inverse participation ratio $\mathfrak{I}$ (IPR), defined in the following way [86]

$$\mathfrak{I} = \left(\sum_m |\psi_m|^4\right)\left(\sum_m |\psi_m|^2\right)^{-2}. \tag{C.1}$$

Here, ψ_m represents a mode amplitude on site m in the 1D system. The mode corresponds to e.g., a field strength, voltage, pressure, or other relevant physical quantities characteristic to a physical implementation under consideration. The summation is performed over all N sites within the chain.

Appendix D. Derivation of coupling strength formula

Consider a two-waveguide coupler with a Hamiltonian in the basis of individual waveguide modes:

$$\mathcal{H} = \begin{pmatrix} \beta_0 & c \\ c & \beta_0 \end{pmatrix}, \tag{D.1}$$

where:

- β_0 is the propagation constant of the individual waveguides
- c is the coupling strength between the waveguides

To solve the eigenvalue problem, we consider the characteristic equation $\det(\mathcal{H} - \lambda I) = 0$. Expanding this determinant gives:

$$(\beta_0 - \lambda)^2 - c^2 = 0 \tag{D.2}$$

The eigenvalues $\lambda_{\pm}$ represent the two propagation constants β_1 and β_2:

$$|c| = \beta_0 - \beta_1 \tag{D.3}$$

$$|c| = \beta_2 - \beta_0 \tag{D.4}$$

Multiplying these equations and taking the square gives the resulting formula:

$$|c| = \sqrt{(\beta_0 - \beta_1)(\beta_2 - \beta_0)}. \tag{D.5}$$

Data availability

Data will be made available on request.

References

[1] M. Hasan, C.Kane, Colloquium: topological insulators, Rev. Mod. Phys. 82 (2010) 3045–3067, https://link.aps.org/doi/10.1103/RevModPhys.82.3045.

[2] X. Qi, S. Zhang, Topological insulators and superconductors, Rev. Mod. Phys. 83 (2011) 1057–1110, https://link.aps.org/doi/10.1103/RevModPhys.83.1057.

[3] K. Klitzing, T. Chakraborty, P. Kim, V. Madhavan, X. Dai, J. McIver, Y. Tokura, L. Savary, D. Smirnova, A. Rey, C. Felser, J. Gooth, X. Qi, 40 years of the quantum Hall effect, Nat. Rev. Phys. 2 (2020) 397–401, https://doi.org/10.1038/s42254-020-0209-1.

[4] C. Chang, C. Liu, A. MacDonald, Colloquium: quantum anomalous Hall effect, Rev. Mod. Phys. 95 (2023) 011002, https://link.aps.org/doi/10.1103/RevModPhys.95.011002.

[5] S. Elliott, M. Franz, Colloquium: Majorana fermions in nuclear, particle, and solid-state physics, Rev. Mod. Phys. 87 (2015) 137–163, https://link.aps.org/doi/10.1103/RevModPhys.87.137.

[6] M. Hasan, G. Chang, I. Belopolski, G. Bian, S. Xu, J. Yin, Weyl, Dirac and high-fold chiral fermions in topological quantum matter, Nat. Rev., Mater. 6 (2021) 784–803, https://doi.org/10.1038/s41578-021-00301-3.

[7] D. Nenno, C. Garcia, J. Gooth, C. Felser, P. Narang, Axion physics in condensed-matter systems, Nat. Rev. Phys. 2 (2020) 682–696, https://doi.org/10.1038/s42254-020-0240-2.

[8] A. Kitaev, Fault-tolerant quantum computation by anyons, Ann. Phys. 303 (2003) 2–30, https://www.sciencedirect.com/science/article/pii/S0003491602000180.

[9] C. Nayak, S. Simon, A. Stern, M. Freedman, S. Das Sarma, Non-Abelian anyons and topological quantum computation, Rev. Mod. Phys. 80 (2008) 1083–1159, https://link.aps.org/doi/10.1103/RevModPhys.80.1083.

[10] J. Pachos, Introduction to Topological Quantum Computation, Cambridge University Press, 2012.

[11] P. Boross, J. Asbóth, G. Széchenyi, L. Oroszlány, A. Pályi, Poor man's topological quantum gate based on the Su-Schrieffer-Heeger model, Phys. Rev. B 100 (2019) 045414, https://link.aps.org/doi/10.1103/PhysRevB.100.045414.

[12] V. Lahtinen, J. Pachos, A short introduction to topological quantum computation, SciPost Phys. 3 (2017) 021, https://scipost.org/10.21468/SciPostPhys.3.3.021.

[13] S. Mittal, V. Orre, M. Hafezi, Topologically robust transport of entangled photons in a 2D photonic system, Opt. Express 24 (2016) 15631–15641, https://opg.optica.org/oe/abstract.cfm?URI=oe-24-14-15631.

[14] M. Rechtsman, Y. Lumer, Y. Plotnik, A. Perez-Leija, A. Szameit, M. Segev, Topological protection of photonic path entanglement, Optica 3 (2016) 925–930, https://opg.optica.org/optica/abstract.cfm?URI=optica-3-9-925.

[15] S. Boutin, P. Lopes, A. Mu, U. Mendes, I. Garate, Topological Josephson bifurcation amplifier: semiclassical theory, J. Appl. Phys. 129 (2021) 214302, https://doi.org/10.1063/5.0050672.

[16] J. Alicea, Y. Oreg, G. Refael, F. Oppen, M. Fisher, Non-Abelian statistics and topological quantum information processing in 1D wire networks, Nat. Phys. 7 (2011) 412–417, https://doi.org/10.1038/nphys1915.

[17] A. Blanco-Redondo, B. Bell, D. Oren, B. Eggleton, Mordechai Segev, Topological protection of biphoton states, Science 362 (2018) 568–571, https://www.science.org/doi/abs/10.1126/science.aau4296.

[18] F. Flamini, N. Spagnolo, F. Sciarrino, Photonic quantum information processing: a review, Rep. Prog. Phys. 82 (2018) 016001, https://doi.org/10.1088/1361-6633/aad5b2.

[19] H. Xue, Y. Yang, B. Zhang, Topological valley photonics: physics and device applications, Adv. Photonics Res. 2 (2021) 2100013, https://doi.org/10.1002/adpr.202100013.

[20] H. Price, Y. Chong, A. Khanikaev, H. Schomerus, L. Maczewsky, M. Kremer, M. Heinrich, A. Szameit, O. Zilberberg, Y. Yang, B. Zhang, A. Alù, R. Thomale, I. Carusotto, P. St-Jean, A. Amo, A. Dutt, L. Yuan, S. Fan, X. Yin, C. Peng, T. Ozawa, A.A. Blanco-Redondo, Roadmap on topological photonics, J. Phys.: Photonics 4 (2022), https://doi.org/10.1088/2515-7647/ac4ee4.

[21] A. Kumar, M. Gupta, P. Pitchappa, Y. Tan, N. Wang, R. Singh, Topological sensor on a silicon chip, Appl. Phys. Lett. 121 (2022) 011101, https://doi.org/10.1063/5.0097129.

[22] F. Koch, J. Budich, Quantum non-Hermitian topological sensors, Phys. Rev. Res. 4 (2022) 013113, https://link.aps.org/doi/10.1103/PhysRevResearch.4.013113.

[23] V. Puchnin, O. Matvievskaya, A. Slobozhanyuk, A. Shchelokova, N. Olekhno, Application of topological edge states in magnetic resonance imaging, Phys. Rev. Appl. 20 (2023) 024076, https://link.aps.org/doi/10.1103/PhysRevApplied.20.024076.

[24] W. Su, J. Schrieffer, A. Heeger, Solitons in polyacetylene, Phys. Rev. Lett. 42 (1979) 1698–1701, https://doi.org/10.1103/PhysRevLett.42.1698.

[25] H. Takayama, Y. Lin-Liu, K. Maki, Continuum model for solitons in polyacetylene, Phys. Rev. B 21 (1980) 2388–2393, https://link.aps.org/doi/10.1103/PhysRevB.21.2388.

[26] S. Ryu, Y. Hatsugai, Topological origin of zero-energy edge states in particle-hole symmetric systems, Phys. Rev. Lett. 89 (2002) 077002, https://link.aps.org/doi/10.1103/PhysRevLett.89.077002.

[27] L. Li, Z. Xu, S. Chen, Topological phases of generalized Su-Schrieffer-Heeger models, Phys. Rev. B 89 (2014) 085111, https://link.aps.org/doi/10.1103/PhysRevB.89.085111.

[28] M. Maffei, A. Dauphin, F. Cardano, M. Lewenstein, P. Massignan, Topological characterization of chiral models through their long time dynamics, New J. Phys. 20 (2018) 013023, https://doi.org/10.1088/1367-2630/aa9d4c.

[29] J. Ryu, S. Woo, N. Myoung, H. Park, Topological edge states in bowtie ladders with different cutting edges, Physica E, Low-Dimens. Syst. Nanostruct. 137 (2022) 114941, https://www.sciencedirect.com/science/article/pii/S1386947721003131.

[30] C. Lee, I. Io, Hsien Kao, Winding number and Zak phase in multi-band SSH models, Chin. J. Phys. 78 (2022) 96–110, https://www.sciencedirect.com/science/article/pii/S0577907322001381.

[31] B. Pérez-González, M. Bello, Á. Gómez-León, G. Platero, Interplay between long-range hopping and disorder in topological systems, Phys. Rev. B 99 (2019) 035146, https://link.aps.org/doi/10.1103/PhysRevB.99.035146.

[32] T. Du, Y. Li, H. Lu, H. Zhang, One-dimensional extended Su–Schrieffer–Heeger models as descendants of a two-dimensional topological model, New J. Phys. 26 (2024) 023044, https://doi.org/10.1088/1367-2630/ad2896.

[33] M. Verbin, O. Zilberberg, Y. Kraus, Y. Lahini, Y. Silberberg, Observation of topological phase transitions in photonic quasicrystals, Phys. Rev. Lett. 110 (2013) 076403, https://link.aps.org/doi/10.1103/PhysRevLett.110.076403.

[34] Y. Kraus, O. Zilberberg, Quasiperiodicity and topology transcend dimensions, Nat. Phys. 12 (2016) 624–626, https://doi.org/10.1038/nphys3784.

[35] O. Zilberberg, Topology in quasicrystals, Opt. Mater. Express 11 (2021) 1143–1157, https://opg.optica.org/ome/abstract.cfm?URI=ome-11-4-1143.

[36] S. Aubry, G. André, Analyticity breaking and Anderson localization in incommensurate lattices, Ann. Isr. Phys. Soc. 3 (1980) 18.

[37] Y. Kraus, Y. Lahini, Z. Ringel, M. Verbin, O. Zilberberg, Topological states and adiabatic pumping in quasicrystals, Phys. Rev. Lett. 109 (2012) 106402, https://link.aps.org/doi/10.1103/PhysRevLett.109.106402.

[38] J. Li, R. Chu, J. Jain, S. Shen, Topological Anderson insulator, Phys. Rev. Lett. 102 (2009) 136806, https://link.aps.org/doi/10.1103/PhysRevLett.102.136806.

[39] S. Stützer, Y. Plotnik, Y. Lumer, P. Titum, N. Lindner, M. Segev, M. Rechtsman, A. Szameit, Photonic topological Anderson insulators, Nature 560 (2018) 461–465, https://doi.org/10.1038/s41586-018-0418-2.

[40] D. Zhirihin, Y. Kivshar, Topological photonics on a small scale, Small Sci. 1 (2021) 2100065, https://doi.org/10.1002/smsc.202100065.

[41] M. Segev, M. Bandres, Topological photonics: where do we go from here?, Nanophotonics 10 (2021) 425–434, https://doi.org/10.1515/nanoph-2020-0441.

[42] R. Chaunsali, H. Xu, J. Yang, P. Kevrekidis, G. Theocharis, Stability of topological edge states under strong nonlinear effects, Phys. Rev. B 103 (2021) 024106, https://link.aps.org/doi/10.1103/PhysRevB.103.024106.

[43] X. Shi, I. Kiorpelidis, R. Chaunsali, V. Achilleos, G. Theocharis, J. Yang, Disorder-induced topological phase transition in a one-dimensional mechanical system, Phys. Rev. Res. 3 (2021) 033012, https://link.aps.org/doi/10.1103/PhysRevResearch.3.033012.

[44] C. Downing, L. Martín-Moreno, O. Fox, Unconventional edge states in a two-leg ladder, New J. Phys. 26 (2024) 073014, https://doi.org/10.1088/1367-2630/ad5bf9.

[45] J. Gao, Z. Xu, Z. Yang, V. Zwiller, A. Elshaari, Quantum topological photonics with special focus on waveguide systems, Npj Nanophotonics 1 (2024) 34, https://doi.org/10.1038/s44310-024-00034-5.

[46] H. Po, A. Vishwanath, H. Watanabe, Symmetry-based indicators of band topology in the 230 space groups, Nat. Commun. 8 (50) (2017) 50, https://doi.org/10.1038/s41467-017-00133-2.

[47] D. Paszko, D. Rose, M. Szymańska, A.Pal, Edge modes and symmetry-protected topological states in open quantum systems, PRX Quantum 5 (2024) 030304, https://link.aps.org/doi/10.1103/PRXQuantum.5.030304.

[48] T. Hong, T. Chen, D. Jin, Y. Zhu, H. Gao, K. Zhao, T. Zhang, W. Ren, G. Cao, Discovery of new topological insulators and semimetals using deep generative models, npj Quantum Mater. 10 (2025) 12, https://doi.org/10.1038/s41535-025-00731-0.

[49] W. Benalcazar, B. Bernevig, L. Taylor, Hughes quantized electric multipole insulators, Science 357 (2017) 61–66, https://www.science.org/doi/abs/10.1126/science.aah6442.

[50] C. Peterson, W. Benalcazar, T. Hughes, G. Bahl, A quantized microwave quadrupole insulator with topologically protected corner states, Nature 555 (2018) 346–350, https://doi.org/10.1038/nature25777.

[51] N. Fu, Z. Fu, H. Zhang, Q. Liao, D. Zhao, S. Ke, Topological bound modes in optical waveguide arrays with alternating positive and negative couplings, Opt. Quantum Electron. 52 (2020) 61, https://doi.org/10.1007/s11082-019-2178-0.

[52] M. Kremer, I. Petrides, E. Meyer, M. Heinrich, O. Zilberberg, A. Szameit, A square-root topological insulator with non-quantized indices realized with photonic Aharonov-Bohm cages, Nat. Commun. 11 (2020) 907, https://doi.org/10.1038/s41467-020-14692-4.

[53] X. Ni, M. Li, M. Weiner, A. Alù, A. Khanikaev, Demonstration of a quantized acoustic octupole topological insulator, Nat. Commun. 11 (2020) 2108, https://doi.org/10.1038/s41467-020-15705-y.

[54] D. Liao, Z. Zhang, Y. Cheng, X. Liu, Engineering negative coupling and corner modes in a three-dimensional acoustic topological network, Phys. Rev. B 105 (2022) 184108, https://link.aps.org/doi/10.1103/PhysRevB.105.184108.

[55] V. Kachin, M. Gorlach, Three-dimensional higher-order topological insulator protected by cubic symmetry, Phys. Rev. Appl. 16 (2021) 024032, https://link.aps.org/doi/10.1103/PhysRevApplied.16.024032.

[56] C. Jiang, Y. Song, X. Li, P. Lu, S. Ke, Photonic Möbius topological insulator from projective symmetry in multiorbital waveguides, Opt. Lett. 48 (2023) 2337–2340, https://opg.optica.org/ol/abstract.cfm?URI=ol-48-9-2337.

[57] Z. Liu, G. Wei, H. Wu, J. Xiao, Möbius edge band and Weyl-like semimetal flat-band in topological photonic waveguide array by synthetic gauge flux, Nanophotonics 12 (2023) 3481–3490, https://doi.org/10.1515/nanoph-2023-0311.

[58] J. Dalibard, F. Gerbier, G. Juzeliūinas, P. Öhberg, Colloquium:artificial gauge potentials for neutral atoms, Rev. Mod. Phys. 83 (2011) 1523–1543, https://link.aps.org/doi/10.1103/RevModPhys.83.1523.

[59] X. Li, E. Zhao, W. Vincent Liu, Topological states in a ladder-like optical lattice containing ultracold atoms in higher orbital bands, Nat. Commun. 4 (2013) 1523, https://doi.org/10.1038/ncomms2523.

[60] M. Bellec, U. Kuhl, G. Montambaux, F.Mortessagne, Topological transition of Dirac points in a microwave experiment, Phys. Rev. Lett. 110 (2013) 033902, https://link.aps.org/doi/10.1103/PhysRevLett.110.033902.

[61] S. Nam, A. Taylor, A. Efimov, Diabolical point and conical-like diffraction in periodic plasmonic nanostructures, Opt. Express 18 (2010) 10120–10126, https://opg.optica.org/oe/abstract.cfm?URI=oe-18-10-10120.

[62] J. Zeuner, M. Rechtsman, R. Keil, F. Dreisow, A. Tünnermann, S. Nolte, A. Szameit, Negative coupling between defects in waveguide arrays, Opt. Lett. 37 (2012) 533–535, https://opg.optica.org/ol/abstract.cfm?URI=ol-37-4-533.

[63] R. Keil, C. Poli, M. Heinrich, J. Arkinstall, G. Weihs, H. Schomerus, A. Szameit, Universal sign control of coupling in tight-binding lattices, Phys. Rev. Lett. 116 (2016) 213901, https://link.aps.org/doi/10.1103/PhysRevLett.116.213901.

[64] S. Pocock, X. Xiao, P. Huidobro, V. Giannini, Topological plasmonic chain with retardation and radiative effects, ACS Photonics 5 (2018) 2271–2279, https://doi.org/10.1021/acsphotonics.8b00117.

[65] G. Cáceres-Aravena, L. Torres, R. Vicencio, Topological and flat-band states induced by hybridized linear interactions in one-dimensional photonic lattices, Phys. Rev. A 102 (2020) 023505, https://link.aps.org/doi/10.1103/PhysRevA.102.023505.

[66] J. Schulz, J. Noh, W. Benalcazar, G. Bahl, G. Freymann, Photonic quadrupole topological insulator using orbital-induced synthetic flux, Nat. Commun. 13 (2022) 6597, https://doi.org/10.1038/s41467-022-33894-6.

[67] Y. Qi, C. Qiu, M. Xiao, H. He, M. Ke, Z. Liu, Acoustic realization of quadrupole topological insulators, Phys. Rev. Lett. 124 (2020) 206601, https://link.aps.org/doi/10.1103/PhysRevLett.124.206601.

[68] A. Dutt, M. Minkov, I. Williamson, S. Fan, Higher-order topological insulators in synthetic dimensions, Light: Sci. Appl. 9 (2020) 131, https://doi.org/10.1038/s41377-020-0334-8.

[69] X. Ni, A. Alù, Higher-order topolectrical semimetal realized via synthetic gauge fields, APL Photon. 6 (2021) 050802, https://doi.org/10.1063/5.0041458.

[70] J. Bao, D. Zou, W. Zhang, W. He, H. Sun, X. Zhang, Topoelectrical circuit octupole insulator with topologically protected corner states, Phys. Rev. B 100 (2019) 201406(R).

[71] S. Liu, S. Ma, Q. Zhang, L. Zhang, C. Yang, O. You, W. Gao, Y. Xiang, T. Cui, S. Zhang, Octupole corner state in a three-dimensional topological circuit, Light: Sci. Appl. 9 (2020) 145, https://doi.org/10.1038/s41377-020-00381-w.

[72] S. Mukherjee, M. Di Liberto, P. Öhberg, R. Thomson, N. Goldman, Experimental observation of Aharonov-Bohm cages in photonic lattices, Phys. Rev. Lett. 121 (2018) 075502, https://link.aps.org/doi/10.1103/PhysRevLett.121.075502.

[73] C. Jörg, G. Queraltó, M. Kremer, G. Pelegrí, J. Schulz, A. Szameit, G. Von Freymann, J. Mompart, V. Ahufinger, Artificial gauge field switching using orbital angular momentum modes in optical waveguides, Light: Sci. Appl. 9 (2020) 150, https://doi.org/10.1038/s41377-020-00385-6.

[74] A. Gorbach, J. Beer, A. Souslov, Topological edge states in equidistant arrays of lithium niobate nano-waveguides, Opt. Lett. 48 (2023) 1982–1985, https://opg.optica.org/ol/abstract.cfm?URI=ol-48-8-1982.

[75] R. Savelev, M. Gorlach, Topological states in arrays of optical waveguides engineered via mode interference, Phys. Rev. B 102 (2020) 161112, https://link.aps.org/doi/10.1103/PhysRevB.102.161112.

[76] D. Guzmán-Silva, G. Cáceres-Aravena, R. Vicencio, Experimental observation of interorbital coupling, Phys. Rev. Lett. 127 (2021) 066601, https://link.aps.org/doi/10.1103/PhysRevLett.127.066601.

[77] G. Cáceres-Aravena, D. Guzmán-Silva, I. Salinas, R. Vicencio, Controlled transport based on multiorbital Aharonov-Bohm photonic caging, Phys. Rev. Lett. 128 (2022) 256602, https://link.aps.org/doi/10.1103/PhysRevLett.128.256602.

[78] M. Mazanov, D. Román-Cortés, G. Cáceres-Aravena, C. Cid, M. Gorlach, R. Vicencio, Photonic molecule approach to multiorbital topology, Nano Lett. 24 (2024) 4595–4601, https://doi.org/10.1021/acs.nanolett.4c00728.

[79] G. Cáceres-Aravena, M. Nedić, P. Vildoso, G. Gligorić, J. Petrovic, A. Maluckov, R. Vicencio, Compact topological edge states in flux-dressed graphenelike photonic lattices, Phys. Rev. Lett. 133 (2024) 116304, https://link.aps.org/doi/10.1103/PhysRevLett.133.116304.

[80] Z. Jiao, S. Longhi, X. Wang, J. Gao, W. Zhou, Y. Wang, Y. Fu, L. Wang, R. Ren, L. Qiao, X. Jin, Experimentally detecting quantized Zak phases without chiral symmetry in photonic lattices, Phys. Rev. Lett. 127 (2021) 147401, https://link.aps.org/doi/10.1103/PhysRevLett.127.147401.

[81] Z. Liu, Q. Zhang, Y. Chen, J. Xiao, General coupled-mode analysis of a geometrically symmetric waveguide array with nonuniform gain and loss, Photon. Res. 5 (2017) 57–63, https://doi.org/10.1364/PRJ.5.000057.

[82] G. Cáceres-Aravena, B. Real, D. Guzmán-Silva, A. Amo, L. Foa Torres, R. Vicencio, Experimental observation of edge states in SSH-Stub photonic lattices, Phys. Rev. Res. 4 (2022) 013185, https://link.aps.org/doi/10.1103/PhysRevResearch.4.013185.

[83] M. Maffei, A. Dauphin, F. Cardano, M. Lewenstein, P. Massignan, Topological characterization of chiral models through their long time dynamics, New J. Phys. 20 (2018) 013023.

[84] K. Padavić, S. Hegde, W. DeGottardi, S. Vishveshwara, Topological phases, edge modes, and the Hofstadter butterfly in coupled Su-Schrieffer-Heeger systems, Phys. Rev. B 98 (2018) 024205, https://link.aps.org/doi/10.1103/PhysRevB.98.024205.

[85] X. Deng, C. Lai, C. Chien, Superconducting circuit simulator of Bose-Hubbard model with a flat band, Phys. Rev. B 93 (2016) 054116, https://link.aps.org/doi/10.1103/PhysRevB.93.054116.

[86] D. Thouless, Electrons in disordered systems and the theory of localization, Phys. Rep. 13 (1974) 93–142, https://www.sciencedirect.com/science/article/pii/0370157374900295.